Stability Analysis and Robust Design of *LCL* With Multituned Traps Filter for Grid-Connected Converters

Majid Sanatkar-Chayjani, *Student Member, IEEE*, and Mohammad Monfared, *Senior Member, IEEE*

***Abstract*—Utilizing high-order passive filters for the voltage-source converters is becoming attractive in industrial applications due to the excellent attenuation performance, smaller size, and lower cost. The *LCL*, the multituned traps, and recently the combined *LCL* with multituned traps (*LCL-mT*) are the most popular high-order filters. However, the increased number of elements and the inherent resonances complicate both filter parameter design and current control loop stabilization, especially, in the presence of parameter uncertainties and wide variations of the grid inductance. Hence, in this paper a straightforward and robust design procedure for the *LCL-mT* filter is proposed. Compared to the existing methods, the proposed technique is not iterative and satisfies the traditional practical limits on filter parameters, while ensures stability even in the presence of wide grid inductance variations and filter parameter uncertainties. The validity and effectiveness of the proposed method are proved by simulation and experimental results.**

***Index Terms*—Delay-based stabilization, *LCL* and traps filters, single-loop control, voltage-source converter.**

I. Introduction

EVER increasing energy demands along with rising cost and environmental concerns about conventional energy resources have attracted considerable attention to distributed generation powered by renewable resources. The generated power in distributed generation systems is normally injected to the power grid by voltage-source converters (VSCs) [1], [2]. In order to attenuate the switching harmonics and generate a high-quality sinusoidal current waveform, VSCs are connected to the grid through a low-pass filter. This filter is traditionally a simple inductance. Compared to the simple *L* filter, the higher order filters, such as *LCL*, multituned traps, and combination of them, offer better attenuation performance with lower total inductance, which may considerably reduce the volume and the total cost of the filter [3]–[6].

However, the inherent resonance of high-order filters challenges the stability of the current control loop. To tackle the instability problem, several methods including passive damping, active damping, and delay-based stabilization have been already presented [3]–[22]. Passive damping is the simplest, which ensures stability by adding a resistor to the filter structure at the price of reduced efficiency [7], [8]. Several active damping methods are already proposed to ensure stability, while avoiding the additional losses [9]–[17]. In these methods, damping is achieved at the price of using extra sensors [9]–[14] or digital filters [15], [16]. Also, the control is more complicated, especially when considering the digital implementation delays [12]–[14].

Another interesting active damping technique is just based on the inherent delay of the digital control systems [18]–[21]. Accordingly, a simple single-loop current controlled VSC is stable if the resonance frequency, $\omega_{\rm res}$, lies in the range $\omega_s/6 < \omega_{\rm res} < \omega_s/2$ (for grid current feedback) [18], [19] and $\omega_{\rm res} < \omega_s/6$ or $\omega_{\rm res} > \omega_s/2$ (for converter current feedback) [20]–[22], in which ω_s is the sampling frequency. Evidently, the delay-based stabilization is sensitive to grid impedance variations and uncertainties in filter parameters, which may push the resonance frequency outside its stable range.

To even more reduce the filter volume and cost, the insertion of multiple *LC* resonance branches (traps) in parallel with the capacitor of the *LCL* filter is recently proposed [5], [6]. In the *LCL* filter with multituned traps (*LCL-mT*), the *LCL* filter offers the excellent characteristics of –60 dB/dec roll-off at high frequencies and at the same time the traps provide significant attenuation around the switching sideband frequencies. This filter is applicable to converters with low to medium switching frequencies, where the switching sideband frequencies are relatively close to the fundamental frequency. In this situation, an effective harmonics filtering by the conventional filters may affect the fundamental component. The other potential application, as recommended by [5], is for the converters with a low converter side inductor. While the *LCL-mT* combines the advantages of both *LCL* and traps filters, it is a complicated and difficult task to design the filter parameters and stabilize the current control system, especially if the number of traps increases. In [5], a design procedure for the *LCL-mT* filter is presented, in which the filter elements are chosen in accordance to some practical criteria including the converter current ripple, the filter reactive power and the grid current harmonics. However, the capacitors are chosen arbitrary. In [6], a design method for the *LCL-mT* filter with one trap, called *LCL-LC*, is also presented. The resonance frequency characteristic is approximated, then, the filter parameters are selected. In both [5] and [6], the passive damping is used for stability, which introduces extra losses.

Manuscript received January 20, 2016; revised April 14, 2016; accepted May 5, 2016. Date of publication June 21, 2016; date of current version October 7, 2016.

The authors are with the Department of Electrical Engineering, Faculty of Engineering, Ferdowsi University of Mashhad, Mashhad 91779-48974, Iran (e-mail: majid.sanatkar@stu.um.ac.ir; m.monfared@um.ac.ir).

Color versions of one or more of the figures in this paper are available online at http://ieeexplore.ieee.org.

Digital Object Identifier 10.1109/TIE.2016.2582792

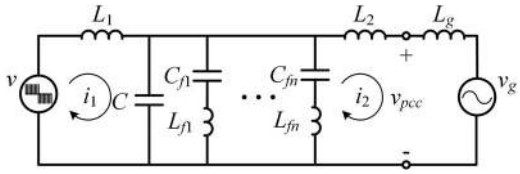

Fig. 1. Grid-connected converter with *LCL-mT* filter.

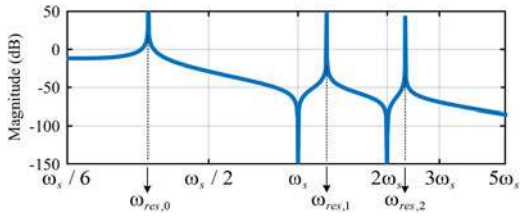

Fig. 2. Bode magnitude plot of $G_{i2}(s)$.

In this paper, first the stability conditions, by means of the delay-based stabilization method, for the traps resonance frequencies are explored, taking into account the folding effect of the digital system. Then, the resonance frequencies of the *LCL-mT* filter without any approximation are determined, which are used for the filter parameter design. Afterward, a filter design procedure, simultaneously considering some practical criteria, such as the limits on the converter current ripple and the grid current harmonics, and stability conditions of the resonance frequencies, is proposed. The proposed filter design algorithm is also robust against a wide range of grid inductance variations and filter elements uncertainties. The theoretical achievements are supported by extensive simulation and practical experiments.

II. Modeling of *LCL-mT* Filter

Fig. 1 shows a single-phase VSC, which is connected to the grid through an *LCL-mT* filter. In the *LCL-mT* filter multiple L_fC_f traps are connected in parallel with the capacitor branch of the conventional *LCL* filter. The *LCL-mT* filter combines the advantages of both *LCL* and tuned trap filters, in which the *LCL* filter offers the excellent characteristics of – 60 dB/dec roll-off at high frequencies and each trap provides significant attenuation around its tuned frequency. The traps are properly tuned at multiples of the switching frequency (switching sidebands).

In Fig. 1, (L_1, L_2, C) and $(L_{f,i}, C_{f,i})$ are the parameters of *LCL* and ith trap, respectively. By neglecting the equivalent series resistance (ESR) of filter components, the transfer function of the converter output voltage to the grid current can be written as

$$G_{i2}(s) = \frac{i_2(s)}{v(s)} = \frac{1}{L_1L'_2Cs(s^2+\omega_{\text{res},0}^2)} \prod_{i=1}^{n} \frac{(s^2+\omega_{f,i}^2)}{(s^2+\omega_{\text{res},i}^2)} \tag{1}$$

where $L'_2 = L_2 + L_g$ and L_g represents the equivalent inductance of the grid and $\omega_{f,i}$ is the tuned frequency of the ith trap. For the single-phase VSC with the unipolar pulse width modulation (PWM), the sideband harmonics are located at even multiples of the switching frequency $(2\omega_{\text{sw}}, 4\omega_{\text{sw}}, \ldots)$. By adopting the asymmetrical (or double-update) sampling technique, the sampling frequency is twice the switching frequency $(\omega_s = 2\omega_{\text{sw}})$, consequently $\omega_{f,i}s$ are selected as ω_s, $2\omega_s$, etc.

The $\omega_{\text{res},0}$ and $\omega_{\text{res},i}$ are the resonance frequencies of the *LCL* and traps, respectively. It should be noted that these resonance frequencies are dependent on parameters of the *LCL-mT* filter with complicated relationships [6]. As an example, the Bode magnitude plot of $G_{i2}(s)$ with $n = 2$ is plotted in Fig. 2. As seen, the resonance frequency associated to each trap is located at a slightly higher frequency than its tuned frequency of $\omega_{f,i}$.

III. Single-Loop Current Control and Stability Analysis

In digitally controlled systems, the stability analysis must be directly conducted in the z-domain to provide accurate conclusion. The zero-order hold (ZOH) transform is commonly used for PWM modeling [19]. The z-domain equivalent of $G_{i2}(s)$ with the ZOH transform and the sampling period of $T_s = 1/f_s$ is obtained as

$$\begin{aligned} G_{i2}(z) &= (1-z^{-1})Z\left\{\frac{G_{i2}(s)}{s}\right\} \\ &= \frac{(1-z^{-1})}{L_1L'_2C}Z\left\{\frac{a}{s^2}+\sum_{i=0}^{n}\frac{a_i}{s^2+\omega_{\text{res},i}^2}\right\} \\ &= \frac{1}{L_1L'_2C}\left(\frac{aT_s}{(z-1)}+\sum_{i=0}^{n}\frac{a_i\sin(\omega_{\text{res},i}T_s)\,(z-1)}{\omega_{\text{res},i}\,(z^2-2\cos(\omega_{\text{res},i}T_s)z+1)}\right) \\ &= \frac{N(z)}{(z-1)\prod_{i=0}^{n}(z^2-2\cos(\omega_{\text{res},i}T_s)z+1)} \end{aligned} \tag{2}$$

where a and a_i are functions of $\omega_{f,i}$ and $\omega_{\text{res},i}$, and $N(z)$ is a polynomial of degree $2(n+1)$. The $2(n+1)$ zeros, denoted by $N(z)$, are produced by the ZOH transform from the original poles and zeros of the continuous system. It should be noted that while $G_{i2}(s)$ has $2n$ zeros, $G_{i2}(z)$ has two extra zeros, which are produced by the ZOH transform.

Considering one sample time computation delay, the open-loop transfer function of the grid current controlled converter can be written as

$$G_{\text{ol}}(z) = z^{-1}G_c(z)G_{i2}(z) \tag{3}$$

where, $G_c(z)$ is the controller transfer function in z-domain, which is a proportional resonant (PR) controller. The PR controller can successfully eliminate the steady-state tracking error of sinusoidal references. Taking in mind that the resonant part of the PR controller almost does not affect the frequencies beyond the fundamental, then the controller can be readily considered as a simple proportional gain k_p. With this assumption, the open-loop transfer function (3) can be simplified as

$$G_{\text{ol}}(z) \cong z^{-1}k_pG_{i2}(z). \tag{4}$$

A. Folding Effect

The conjugate pole pairs of $G_{i2}(s)$, which represent $(n+1)$ resonance frequencies of the *LCL-mT* filter, are mapped on the

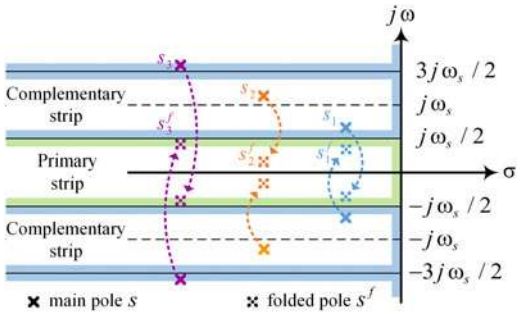

Fig. 3. Folding of conjugate pole pairs with different frequencies (for clarity only the folded poles in the primary strip are shown).

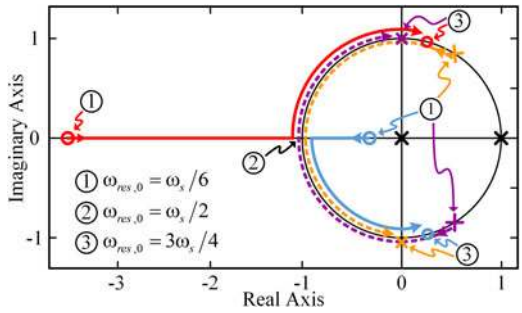

Fig. 4. Trajectory of poles and zeros of $G_{\rm ol}(z)$ with increasing $\omega_{\rm res,0}$ (solid line: zeros trajectory, dashed line: poles trajectory).

unit circle through the ZOH transform. For an s-domain pole with the frequency higher than the Nyquist frequency, the ZOH folds back that pole into a frequency lower than the Nyquist frequency [22]. Suppose a system with the s-domain poles at $s=-\sigma\pm j\omega$ with $\omega>\omega_s/2$, through the sampling the folding occurs and the system behaves like a system which had poles at $s=-\sigma\pm j(\omega\pm k\omega_s)$, where $k=1,2,3,\ldots$ Thanks to the low-pass filtering characteristics of the antialiasing filter and the ZOH, the responses due to the folded poles in the complementary strips are well attenuated and, consequently, only the folded poles in the primary strip $(-j\omega_s/2<j\omega<j\omega_s/2)$ are considered here, which are $s^f=-\sigma\pm j\omega^f$ [23], [24]. To better understand the folding effect, Fig. 3 shows an example for three conjugate pole pairs with different frequencies, all beyond the Nyquist frequency. The folded pole pairs in the primary strip are related to the original ones as

$$\begin{cases} s_1=-\sigma_1\pm j\omega_1 & \xrightarrow{\omega_s/2<\omega_1<\omega_s} s_1^f=-\sigma_1\mp j\,|\omega_1-\omega_s| \\ s_2=-\sigma_2\pm j\omega_2 & \xrightarrow{\omega_s<\omega_2<3\omega_s/2} s_2^f=-\sigma_2\pm j\,|\omega_2-\omega_s| \\ s_3=-\sigma_3\pm j\omega_3 & \xrightarrow{3\omega_s/2<\omega_3<2\omega_s} s_3^f=-\sigma_3\mp j\,|\omega_3-2\omega_s| \end{cases} . \tag{5}$$

In general, for a conjugate pole pair with $\omega_{\rm res}>\omega_s/2$, the folded frequency, depending on the original location, is calculated as

$$\left(n-\frac{1}{2}\right)\omega_s<\omega_{\rm res}<\left(n+\frac{1}{2}\right)\omega_s$$
$$\Rightarrow \omega_{\rm res}^f=|n\omega_s-\omega_{\rm res}|\,,n=1,2,\ldots \tag{6}$$

B. Stability Condition for $\omega_{\rm res,0}$

In the delay-based stabilization method, the *LCL* filtered VSC with grid current feedback is stable if the sharp phase change of the *LCL* resonance frequency lies in the range $(-3\pi,-\pi)$. Regarding this limit and considering a total of $1.5T_{\rm s}$ delay, the stable range of the resonance frequency is already obtained as $\omega_s/6<\omega_{\rm res}<\omega_s/2$ [18]. For the case of the *LCL-mT* filter, the same condition also holds for the first resonance frequency, $\omega_{\rm res,0}$. Although, this stable range has already been proven in recent studies, in order to demonstrate the effect of ZOH produced zeros, it is reexamined here. In the following, the effect of ZOH transform on the phase and magnitude characteristic as well as the stability of the system is investigated with Figs. 4 and 5. Fig. 4 shows the trajectory of poles and zeros of (4) with increasing $\omega_{\rm res,0}$ (for more clarity, poles and zeros of traps are not shown). Also, Fig. 5 shows the Bode diagrams of (4) for different values of $\omega_{\rm res,0}$. In order to highlight the folding effect, a comparison between the s-domain open-loop transfer function $G_{\rm ol}(s)=G_c(s)G_{i2}(s)e^{(-1.5T_s s)}$ (solid line) and $G_{\rm ol}(z)$ (dashed line) is given. The $1.5T_s$ delay accounts for one and half sample delays of computations and PWM.

In Fig. 4 and for $\omega_{\rm res,0}<\omega_s/2$, the zeros created by the ZOH are located at negative side of the real axis (between ① and ②) and have negligible effect on the Bode plot of the discrete system, as evident in Fig. 5(a). In this case, only when the resonance frequency is very close to $\omega_s/2$ the effect of zeros appears as a small deviation on the magnitude characteristic with no contribution on the phase, as shown in Fig. 5(b). As already expected, the system remains stable. With $\omega_{\rm res,0}=\omega_s/2$ both pole pairs and zeros are placed at $z=-1$ (at ②) and as shown in Fig. 5(c) cancel each other. As it can be seen in Fig. 4, by increasing $\omega_{\rm res,0}$ above $\omega_s/2$, the zeros transform to a pair of conjugate zeros on the unit circle (between ② and ③) with the frequency always smaller than the folded pole pair frequency, $\omega_{\rm res,0}^f$. Consequently, as it can be detected in Fig. 5 (d), the zeros drive the phase out of the stable range of $(-3\pi,-\pi)$ and lead to instability.

C. Stability Condition for Traps

As shown in Fig. 2, the ith trap produces conjugate pairs of zeros and poles at and above the ith switching sideband, respectively. In the discretizing process, the pole pair is folded to $\omega_{{\rm res},i}^f$ according to (6). Furthermore, as it can be seen in Fig. 6, in the vicinity of the folded poles, a pair of zeros is also produced by the ZOH, which can have a slightly higher or lower frequency than $\omega_{{\rm res},i}^f$. In the following, the combined effect of the folded pole pair and the produced zero pair on the stability of the digital control system is investigated by Fig. 6. For the sake of simplicity, only the first trap is considered in this figure.

As it can be seen in Fig. 2, the first trap resonance frequency is higher than the first sideband frequency, i.e., $\omega_{\rm res,1}>\omega_s$. Given the value of resonance frequency, the stability of the closed-loop system is determined as follows.

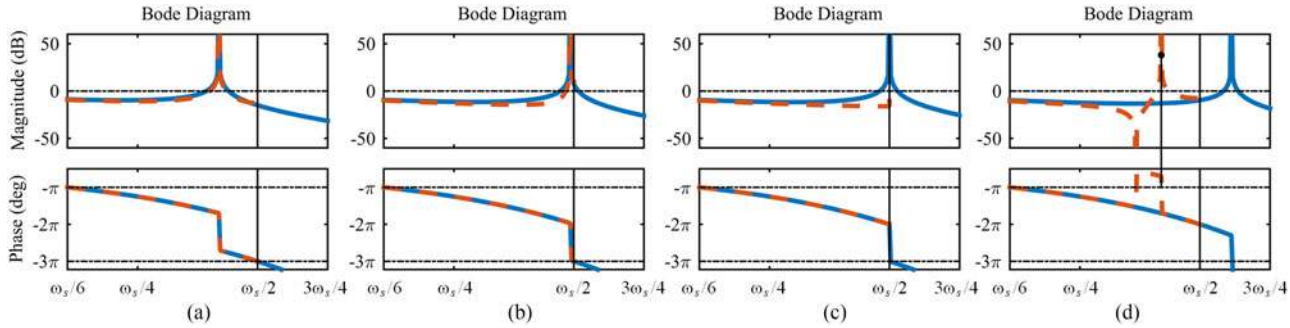

Fig. 5. Bode diagrams of *LCL-mT* filtered VSC with different values of resonance frequency (dashed line: $G_{\rm ol}(z)$, solid line: $G_{\rm ol}(s) = G_c(s)G_{i2}(s)e^{(-1.5T_s s)}$) (a) $\omega_{\rm res,0} = 0.4\omega_s$, (b) $\omega_{\rm res,0} = 0.49\omega_s$, (c) $\omega_{\rm res,0} = 0.5\omega_s$, (d) $\omega_{\rm res,0} = 0.6\omega_s$.

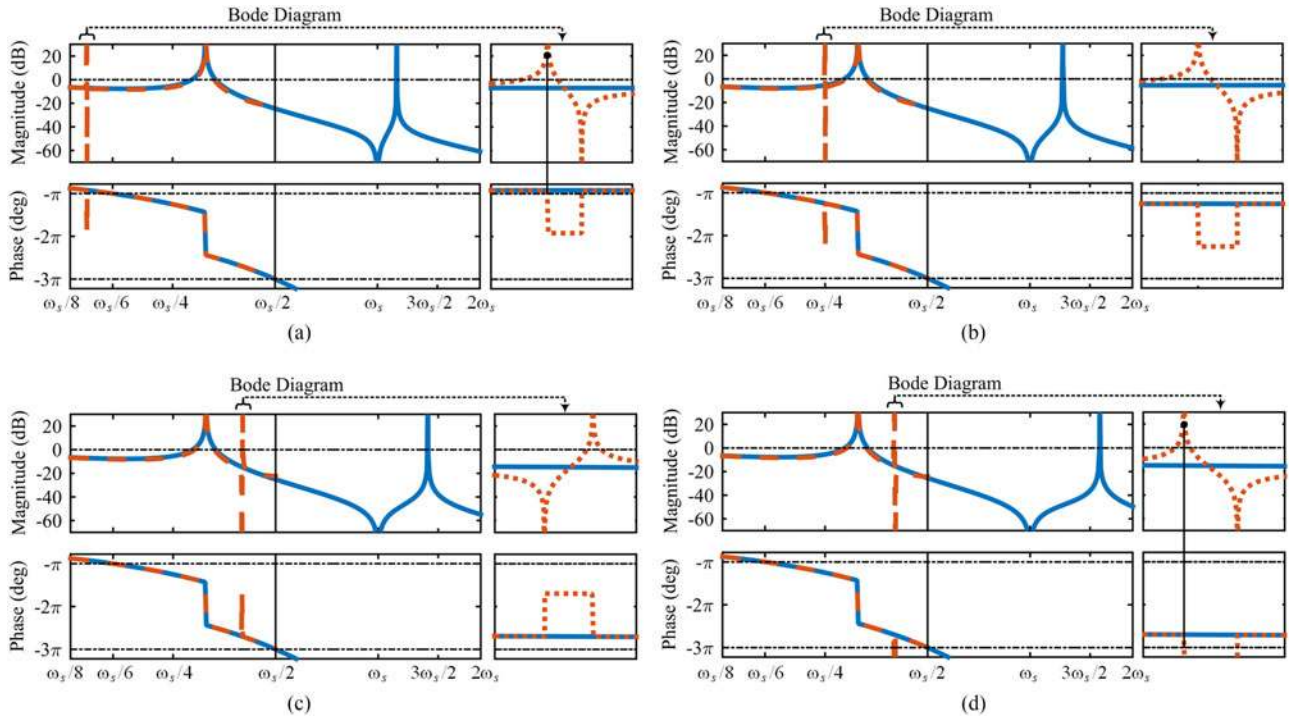

Fig. 6. Bode diagrams of *LCL-mT* filtered VSC with different values of resonance frequency (dashed line: $G_{\rm ol}(z)$, solid line: $G_{\rm ol}(s) = G_c(s)G_{i2}(s)e^{(-1.5T_s s)}$) (a) $\omega_{\rm res,1} = 1.14\omega_s(\omega^f_{\rm res,1} = 0.14\omega_s)$, (b) $\omega_{\rm res,1} = 1.25\omega_s(\omega^f_{\rm res,1} = 0.25\omega_s)$, (c) $\omega_{\rm res,1} = 1.4\omega_s(\omega^f_{\rm res,1} = 0.4\omega_s)$, and (d) $\omega_{\rm res,1} = 1.6\omega_s(\omega^f_{\rm res,1} = 0.4\omega_s)$.

1) $\omega_s < \omega_{\rm res,1} < 7\omega_s/6$ $(0 < \omega^f_{\rm res,1} < \omega_s/6)$: As it can be seen in Fig. 6(a), the sharp phase change of the folded resonance frequency occurs out of the stable range of $(-3\pi, -\pi)$ and the closed-loop system will be unstable.
2) $7\,\omega_s/6 < \omega_{\rm res,1} < 3\omega_s/\,2\,(\omega_s/\,6 < \omega^f_{\rm res,1} < \omega_s/2)$: The Bode diagrams for this case are shown in Fig. 6(b) and (c). Regardless of the ratio between $\omega^f_{\rm res,1}$ and $\omega_{\rm res,0}$, the sharp phase change remains inside $(-3\pi, -\pi)$ and the closed-loop system is stable.
3) $3\omega_s/2 < \omega_{\rm res,1}$ $(\omega_s/2 > \omega^f_{\rm res,1})$: By increasing $\omega_{\rm res,1}$, once it goes beyond $3\omega_s/2, \omega^f_{\rm res,1}$ begins to decrease and as shown in Fig. 6 (d), the sharp phase change of the folded resonance frequency crosses -3π and consequently the closed-loop system will be unstable.

The same analysis can be performed for other traps. As a general conclusion, the stable range for the $\omega_{{\rm res},i}$ (including $\omega_{\rm res,0}$) can be written as

$$\left(i+\frac{1}{6}\right)\omega_s < \omega_{{\rm res},i} < \left(i+\frac{1}{2}\right)\omega_s, \quad i = 0, 1, \ldots, n. \quad (7)$$

IV. Robust Design of *LCL-mT* Filter

In order to ensure closed-loop stability with no extra resistors, sensors, and complexity the delay-based stabilization method is utilized here. Hence, all resonance frequencies must lie inside the stable region, already defined by (7). However, the most serious problem is the uncertainties due to component tolerances and drifts and also the grid inductance variations, which can

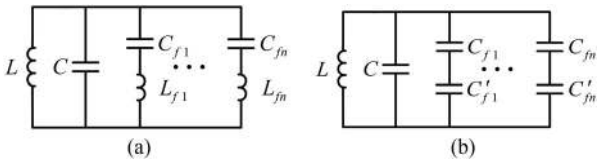

Fig. 7. Simplified circuit of (a) grid-connected converter and (b) L_f replaced with equivalent capacitor to calculate the resonance frequencies.

lead to considerable deviations of the resonance frequencies from the design values. Therefore, as a robust filter design, the filter parameters must be selected in such a way that under all circumstances, all resonance frequencies remain in the stable range.

As already discussed, the filter resonance frequencies determine the stability of the closed-loop system. In the following, the resonance frequencies of the *LCL-mT* filter are derived as a function of the filter parameters.

The resonance frequencies of a circuit are independent of the sources and are only determined by the passive elements and their arrangement in the circuit. Hence, for the sake of simplicity all sources are omitted from the circuit. The *LCL-mT* filtered VSC of Fig. 1, without the sources, simplifies to Fig. 7(a), where $L = L_1||L_2'$. By replacing each L_f with the equivalent capacitor (with an equal impedance $j\omega L_f = 1/(j\omega C_f') : C_f' = -1/(L_f\omega^2)$), the equivalent circuit even more simplifies to Fig. 7(b). The equivalent capacitor of this circuit can be calculated as (8) and consequently an equation for the resonance frequencies can be derived as (9)

$$C_{\text{eq}} = C + \sum_{j=1}^{n} \frac{C_{fj}C'_{fj}}{C_{fj}+C'_{fj}} = C + \sum_{j=1}^{n} \frac{C_{fj}}{1 - L_{fj}C_{fj}\omega^2} \quad (8)$$

$$\omega_{\text{res}}^2 = \frac{1}{L}\left(C + \sum_{j=1}^{n} \frac{C_{fj}}{1 - L_{fj}C_{fj}\omega_{\text{res}}^2}\right)^{-1}. \quad (9)$$

This result is very useful in the filter design stage.

A. Effect of Grid Inductance Variations

Grid inductance variations from 0 to ∞ lead to the resonance frequency change between the values defined by the following equations:

$$\omega_{\text{res,max}}^2 =$$

$$\omega_{\text{res}}^2\big|_{L_g=0} = \frac{1}{(L_1||L_2)}\left(C + \sum_{j=1}^{n} \frac{C_{fj}}{1 - L_{fj}C_{fj}\omega_{\text{res,max}}^2}\right)^{-1} \quad (10)$$

$$\omega_{\text{res,min}}^2 = \omega_{\text{res}}^2\big|_{L_g=\infty} = \frac{1}{L_1}\left(C + \sum_{j=1}^{n} \frac{C_{fj}}{1 - L_{fj}C_{fj}\omega_{\text{res,min}}^2}\right)^{-1}. \quad (11)$$

The minimum and the maximum values of the resonance frequency occur for the maximum and the minimum values of L_g, respectively. The perfect robustness against grid inductance variations is achieved, if the extremum values of each resonance frequency, defined by (10) and (11), remain inside the stable range of (7).

B. Effect of Filter Parameter Uncertainties

Uncertainties such as tolerances and drifts in the passive elements also lead to undesired resonance frequency changes. The actual values of the filter parameters (with subscript "*a*") are assumed to be related to the designed values as $L_a = u_L L$ and $C_a = u_C C$, where u_L and u_C are the uncertainty factors for the inductances and the capacitor, respectively. The elements of traps should have accurate values with very small tolerances. Therefore, the uncertainty effect of the traps elements is neglected. Considering uncertainties, the actual value of the resonance frequency can be written as

$$\omega_{\text{res},a}^2 = \frac{1}{L_a}\left(C_a + \sum_{j=1}^{n} \frac{C_{fj}}{1 - L_{fj}C_{fj}\omega_{\text{res},a}^2}\right)^{-1} = \frac{1}{u_L L}\left(u_C C + \sum_{j=1}^{n} \frac{C_{fj}}{1 - L_{fj}C_{fj}\omega_{\text{res},a}^2}\right)^{-1}. \quad (12)$$

In order to determine the influence of parameter uncertainties on the resonance frequency, an *LCL-mT* filter with one trap is investigated. The resonance frequency of an *LCL-mT* filter with one trap can be calculated as [6]

$$\omega_{\text{res},0\&1} = \sqrt{\frac{b \mp \sqrt{b^2 - 4a}}{2a}} \quad (13)$$

where $a = LCL_{f1}C_{f1}$ and $b = L(C + C_{f1}) + L_{f1}C_{f1}$.

Fig. 8(a) and (b) shows the variations of $\omega_{\text{res},0}$ and $\omega_{\text{res},1}$ as a function of uncertainty factors u_L and u_C by three-dimensional plots. Both uncertainty factors vary from 0.6 to 1.4. For both cases, the resonance frequency variation has an inverse relation to both uncertainty factors, i.e., when both factors are maximum then the minimum value for the resonance frequencies are expected and vice versa. Therefore, the system remains stable if with the worst cases of shifts in the resonance frequencies, they still remain in the stable range.

C. LCL-mT Filter Design

To achieve a robust filter design against the grid inductance variations and filter parameter uncertainties, the stable range of resonance frequency (7) must be met for all resonance frequency variation range determined in previous sections. Furthermore, the designed filter should meet some practical limits, such as the converter current ripple and the grid current harmonics.

In the following, the step-by-step design procedure of the *LCL-mT* filter is suggested. For the sake of simplicity, in the design procedure only one trap for the *LCL-mT* filter is considered. System parameters and design constraints are listed in Table I.

In the first step, the minimum value of L_1 is determined according to the maximum allowed converter current ripple

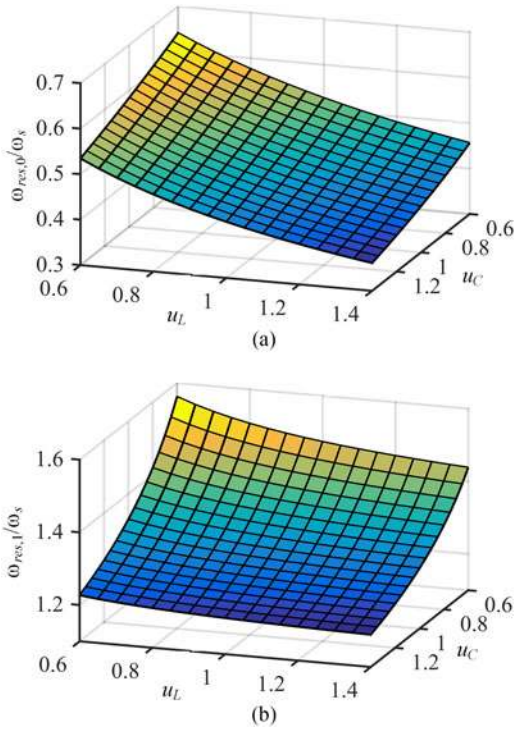

Fig. 8. Resonance frequency variations with uncertainty factors u_L and u_C, (a) $\omega_{\text{res},0}/\omega_s$, (b) $\omega_{\text{res},1}/\omega_s$.

TABLE I
SYSTEM PARAMETERS AND DESIGN CONSTRAINTS

Parameter	Symbol	Value
VSC rated power	S_{rated}	3 kVA
Grid voltage/frequency	V_{rms}/f	$220\text{V}_{\text{rms}}/50\text{Hz}$
DC-link voltage	V_{dc}	380 V
Switching frequency	f_{sw}	5 kHz
Sampling frequency	f_s	10 kHz
Maximum converter current ripple	$\Delta i_{1,\max}$	$0.3I_{P,\text{rated}}$
Uncertainty factor of L_1 and L_2	u_L	1 ± 0.3
Uncertainty factor of C	u_C	1 ± 0.2

$\Delta i_{1,\max}$ as [4]

$$L_{1,\min} = \frac{V_{\text{dc}} T_s}{8\Delta i_{1,\max}}. \tag{14}$$

With the parameters of Table I, $L_{1,\min}$ is calculated as 840 μH.

As already discussed, the maximum decrease in the resonance frequency value occurs with $L_g = \infty$ and the maximum uncertainty factor $u_{\max}$. The resultant minimum resonance frequency can be calculated from (12) as

$$\omega^2_{\text{res},a}\Big|_{\substack{L_g=\infty \\ u=u_{\max}}} = \frac{1}{u_{L,\max}L_1}\left(u_{C,\max}C + \frac{C_{f1}}{1 - L_{f1}C_{f1}\omega^2_{\text{res},a}}\right)^{-1}. \tag{15}$$

To ensure stability for this case, the resultant minimum resonance frequency must be at least equal to the lower limit of the stable range of (7), i.e.,

$$\omega^2_{\text{res},0a}\Big|_{\substack{L_g=\infty \\ u=u_{\max}}} = \left(\frac{\omega_s}{6}\right)^2$$

$$\Rightarrow \frac{1}{u_{L,\max}L_1}\left(u_{C,\max}C + \frac{C_{f1}}{1-(1/6)^2}\right)^{-1} = \left(\frac{\omega_s}{6}\right)^2 \tag{16}$$

$$\omega^2_{\text{res},1a}\Big|_{\substack{L_g=\infty \\ u=u_{\max}}} = \left(\frac{7\omega_s}{6}\right)^2$$

$$\Rightarrow \frac{1}{u_{L,\max}L_1}\left(u_{C,\max}C + \frac{C_{f1}}{1-(7/6)^2}\right)^{-1} = \left(\frac{7\omega_s}{6}\right)^2 \tag{17}$$

where $L_{f1}C_{f1}$ is replaced by $1/\omega_s^2$. By solving this system of linear equations the filter capacitors are calculated as

$$\begin{cases} C = \dfrac{1}{u_{L,\max}u_{C,\max}L_1}\left(\dfrac{6^2}{7\omega_s}\right)^2 \\ C_{f1} = \left(1-(1/6)^2\right)\left((7/6)^2-1\right)u_{C,\max}C \end{cases}. \tag{18}$$

By replacing L_1 with $L_{1,\min}$ from (14) and using parameters in Table I, the C and C_{f1} are calculated as 5.11 and 2.15 μF, respectively. The capacitors are finally chosen to be 5 and 2.1 μF. With the chosen value for C_{f1}, the value of L_{f1} is calculated as 120 μH from $L_{f1} = 1/(C_{f1}\omega_s^2)$. It is worth mentioning that, the reactive power of the capacitors may be another practical criteria that must be met during the design procedure. This limit can be considered as a percent (usually $x = 5\%$) of the base capacitance as $(C_{\text{total}} = C + C_{f1}) \le xC_{\text{base}}$. After the calculation of C and C_{f1} from (18), if $C_{\text{total}} > xC_{\text{base}}$, then C_{total} is limited to xC_{base} and the new values for the capacitors can be calculated as directions of Appendix A.

On the other hand, the system must also remain stable with the maximum increase in the resonance frequency, which occurs with $L_g = 0$ and the minimum uncertainty factor $u_{\min}$. The resultant maximum resonance frequency can be calculated from (12) as

$$\omega^2_{\text{res},a}\Big|_{\substack{L_g=0 \\ u=u_{\min}}} = \frac{1}{u_{L,\min}(L_1||L_2)}\left(u_{C,\min}C + \frac{C_{f1}}{1 - L_{f1}C_{f1}\omega^2_{\text{res},a}}\right)^{-1}. \tag{19}$$

Therefore, the maximum expected value of the resonance frequency must be equal to (or lower than) the upper limit of the stable range of (7), i.e.,

$$\omega^2_{\text{res},0a}\Big|_{\substack{L_g=0 \\ u=u_{\min}}} = \left(\frac{\omega_s}{2}\right)^2$$

$$\Rightarrow \frac{1}{u_{L,\min}(L_1||L_2)}\left(u_{C,\min}C + \frac{C_{f1}}{1-(1/2)^2}\right)^{-1} = \left(\frac{\omega_s}{2}\right)^2 \tag{20}$$

$$\omega^2_{\text{res},1a}\Big|_{\substack{L_g=0 \\ u=u_{\min}}} = \left(\frac{3\omega_s}{2}\right)^2$$

$$\Rightarrow \frac{1}{u_{L,\min}(L_1||L_2)}\left(u_{C,\min}C + \frac{C_{f1}}{1-(3/2)^2}\right)^{-1} = \left(\frac{3\omega_s}{2}\right)^2. \tag{21}$$

TABLE II
COMPARISON OF DESIGNED *LCL-mT* FILTER AND *LCL* FILTER

Filter type	L_1 (Peak rating)	L_2	L_{f1}	C	C_{f1}	LI_P^2	C_{total}	$\frac{\omega_{\text{res},0}}{\omega_s}$	$\frac{\omega_{\text{res},1}}{\omega_s}$
LCL-mT	840 μH(23.5 A)	280 μH(19.5 A)	120 μH(5 A)	5 μF(311 V)	2.1 μF(311 V)	0.57	3.7%	0.4	1.22
LCL	840 μH(23.5 A)	1.5 mH(19.5 A)	–	6.9 μF(311 V)	–	1.03	3.5%	0.26	–

In above equations, all quantities are defined, except L_2. So, by solving (20) and (21) for L_2, it is calculated as 280 and 75 μH, respectively. On the other hand, it can be observed from Fig. 8 that the higher value for L_2 leads to the lower resonance frequency, therefore, one must choose $L_2 = 280$ μH which leads to $\omega_{\text{res},0a} = \omega_s/2$ and $\omega_{\text{res},1a} < 3\omega_s/2$.

There are important limits on the magnitude of harmonic components of the grid current. The IEEE1547.2 2008 standard [25] limits all harmonics higher than 35th to 0.3% of the fundamental component. Considering the high-frequency characteristic of the filter as $G_{i2,\text{HF}}(s) = 1/(L_1L_2Cs^3)$ [8], the value of L_2, which satisfies the current harmonic limit at the second sideband frequency, $\omega_{\text{sb}2} = 2\omega_s$, can be calculated as

$$i_{\text{sb2,max}} = V_{\text{sb2,max}} \left| \frac{1}{L_1L_2Cs^3} \right|_{s=j\omega_{\text{sb}2}} < 0.003I_{P,\text{rated}}$$
$$\Rightarrow L_2 > \frac{V_{\text{sb2,max}}}{0.003I_{P,\text{rated}}L_1C(2\omega_s)^3} \quad (22)$$

where $V_{\text{sb2,max}}$ and $i_{\text{sb2,max}}$ are the maximum values of converter voltage and grid current at the second sideband frequency and $I_{P,\text{rated}}$ is the peak value of the rated converter current. $V_{\text{sb2,max}}$ for the modulation index of 0.8 is approximately equal to 0.12 V_{dc} [26]. Evaluating (22) results in $L_2 > 95$ μH. The maximum value calculated from (20) to (22) is selected as the final value of L_2, which in our case is 280 μH.

The final values of the filter parameters and the peak ratings are listed in Table II. The total value of capacitance is 3.7%, which is lower than the common limit of 5% [4]. A comparison between the *LCL-mT* filter and the *LCL* filter with the same design constraints (i.e., 30% converter current ripple, 0.3% high-frequency component of the grid current and the same stability constraints) is shown in Table II. The grid side inductance for the *LCL-mT* filter is 280 μH (0.5%), which is much smaller than 1.5 mH (2.9%) of the *LCL* filter. The LI_P^2 factor, which is proportional to the volume of the magnetic cores [8], is almost twice for the *LCL* filter, which shows the bigger size of the filter inductors. With the chosen values for the

LCL-mT filter parameters the resonance frequencies are $\omega_{\text{res},0d} = 0.4\omega_s$ and $\omega_{\text{res},1d} = 1.22\omega_s$. To demonstrate the robustness of the proposed design procedure, the expected variation range of the resonance frequencies, along with the stable range defined by (7), are shown in Fig. 9.

For the general case of a *LCL-mT* filter with n traps the same design procedure can be followed, which is presented in Appendix B.

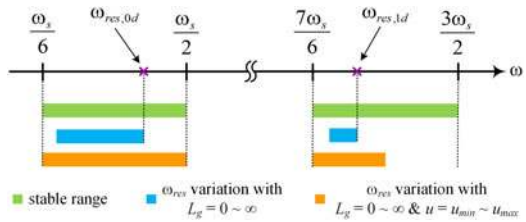

Fig. 9. Resonance frequency variations with L_g and u changes.

V. CURRENT CONTROLER DESIGN CONSIDERING GRID INDUCTANCE VARIATIONS

A. Current Controller Design

In order to eliminate the steady-state tracking error of the sinusoidal reference and also compensate the grid voltage background harmonics, the PR controller with a harmonic compensation (HC) network is used as the current controller. Then, the transfer function of the current controller in the s-domain is

$$G_c(s) = k_p + k_i \sum_{n=1,3,5,\ldots} \frac{s}{s^2 + (n\omega_1)^2}. \quad (23)$$

The gains of the current controller are designed assuming that $L_g = 0$ as $k_p = \omega_{\text{gc}}(L_1 + L_2)$ and $k_i = 0.02k_p\omega_{\text{gc}}$, where ω_{gc} is the desired gain crossover frequency [19]. In order to compensate the grid voltage background harmonics, the resonant terms of the HC are tuned at 3rd-, 5th-, 7th-, 9th-, and 11th-order harmonics. The gain crossover frequency of the current controller is usually selected based on the desired phase margin, speed of dynamic response and the highest HC tuned frequency. Here, the ω_{gc} is selected as $\omega_s/16$, which is upper than the highest HC tuned frequency and results in a phase margin of about $\pi/4$. The Bode diagrams of open-loop transfer function (3) with current controller (23) for different grid inductances are shown in Fig. 10. The impulse invariant method is used to discretize the PR controller and the HC network [27].

B. Effect of Grid Inductance on Controller Performance

As illustrated in Table II, the grid side inductor of the *LCL-mT* filter is usually small compared to the grid inductance L_g, leading to a variable bandwidth characteristics considering the wide variations of L_g, which can challenge the dynamics and even the stability of the current control loop [10]. This situation is really serious in applications with a HC network in the current control loop, where the reduced ω_{gc}, as a result of increased L_g, may become even lower than some HC network resonance frequencies. As can be easily detected in Fig. 10, the direct

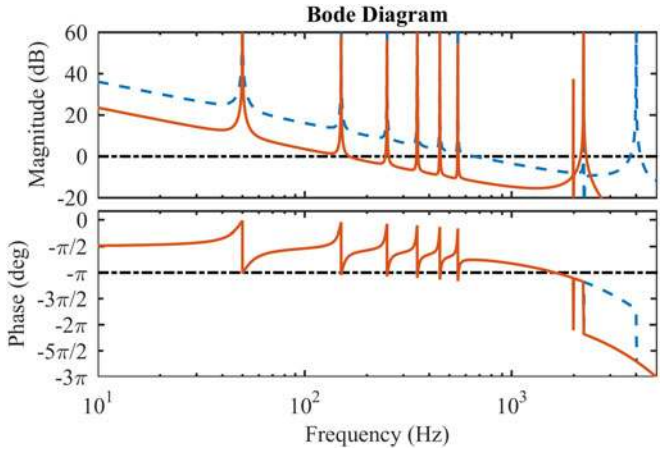

Fig. 10. Bode diagrams of the open-loop transfer function $G_{\rm ol}(z)$ (dashed line: $L_g = 0$, solid line: $L_g = 3.7\text{mH}$).

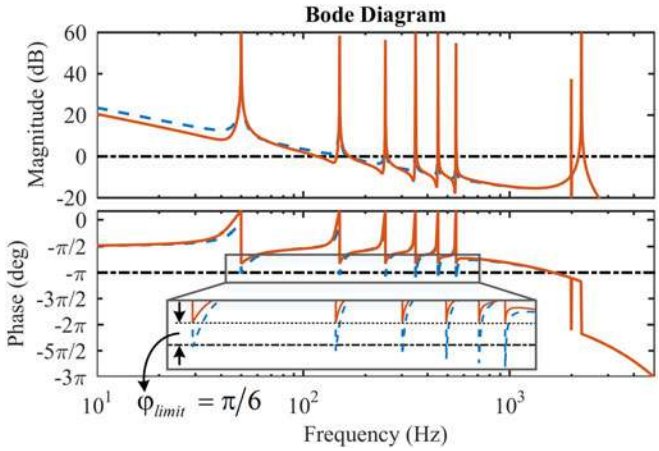

Fig. 11. Bode diagram of open-loop transfer function $G_{\rm ol}(z)$ with $L_g = 3.7\text{mH}$ (dashed line: uncompensated G_c, solid line: compensated G_c).

result is deteriorated stability margins. To alleviate the stability problem in the presence of a high grid inductance, the phase compensated PR+HC is already proposed [28], which is also adopted in this paper as the current controller G_c. The transfer function of the phase compensated G_c in the s-domain is [27]

$$G_c(s) = k_p + k_i \sum_{n=1,3,5,\ldots} \frac{s\cos(\varphi_n) - n\omega_1 \sin(\varphi_n)}{s^2 + (n\omega_1)^2} \quad (24)$$

where φ_n is the phase lead compensation for each resonant controller of G_c. Considering the phase compensation, the sharp phase change of G_c in the vicinity of each tuned frequency (i.e., $n\omega_1$) occurs between $-\pi/2 + \varphi_n$ and $+\pi/2 + \varphi_n$. As it can be seen in Fig. 10 ($\varphi_n = 0$), the highest decrease in the phase of $G_{\rm ol}$ occurs in the vicinity of each tuned frequency of G_c. In order to have a good stability margin around the G_c tuned frequencies, the difference between the phase of $G_{\rm ol}$ and $-\pi$ must be limited to a safe bound, called $\varphi_{\rm limit}$, i.e.,

$$\begin{aligned} &(\angle G_{\rm ol} = \angle G_c + \angle G_{i2} - 1.5T_s\omega)|_{\omega = n\omega_1} = -\pi + \varphi_{\rm limit} \\ &\Rightarrow \left(-\frac{\pi}{2} + \varphi_n\right) + \left(-\frac{\pi}{2}\right) - 1.5T_s n\omega_1 = -\pi + \varphi_{\rm limit} \end{aligned} \quad (25)$$

then, φ_n is calculated as

$$\varphi_n = \varphi_{\rm limit} + 1.5T_s n\omega_1. \quad (26)$$

While $\varphi_{\rm limit}$ can be in the range of 0 to $\pi/2$, a compromise may be $\varphi_{\rm limit} = \pi/6$, which will have a negligible effect on the loop gain at low frequencies. Bode diagrams of $G_{\rm ol}$, with and without the phase compensation of G_c are compared in Fig. 11. It can be seen that the phase compensated controller successfully limits the phase of $G_{\rm ol}$ to $\varphi_{\rm limit} = \pi/6$. Therefore, with increasing L_g, the phase margin will never be under $\pi/6$, which translates to a proper stability margin.

VI. Simulation and Experimental Results

To exhibit the validity of analytical *LCL-mT* filter design procedure, several simulation and experiments have been

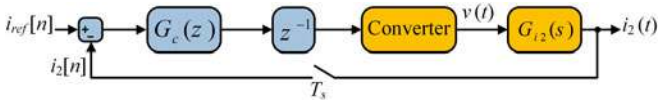

Fig. 12. Block diagram of closed-loop system.

conducted. The block diagram of the studied system is shown in Fig. 12 and the parameters are listed in Table I. The filter parameters are listed in Table II. The PR controller and the HC network gains are selected according to Section V-A recommends, as $k_p = 4.5$ and $k_i = 350$. All resonators are compensated with $\varphi_{\rm limit} = \pi/6$.

Simulations are carried out in PLECS. A 3 kVA laboratory prototype is developed. A Texas Instruments TMS320F28335 floating point digital signal controller is used for implementing the control algorithm.

All simulations are conducted under ideal condition without considering the ESR of filter elements and the resistive part of grid impedance. Hence, the simulation results account for the worst case in terms of damping and stability issues, while in the experimental setup, the presence of ESRs increases the system damping and improves the stability margins.

The steady-state simulated and experimental results for $L_g = 0$ and 3.7 mH are presented in Figs. 13 and 14, respectively. These figures show a good agreement between the results of simulations and experiments. In both cases, the converter system remains stable and maintains the excellent performance even with a large value for the grid inductance. Figs. 13(c) and 14(c) show the grid current harmonic spectrum (with $L_g = 0$). The grid current harmonics around the switching sidebands are well below the 0.3% limit. Furthermore, the grid current Total Harmonic Distortion (THD) in experiments for $L_g = 0$ and 3.7 mH are 2.5% and 2%, respectively, which are far below the 5% limit recommended by the IEEE1547.2 2008 standard.

The converter current and the total current of capacitor and trap branches $(i_C + i_f)$ are shown in Figs. 15–18. The ripple content of the converter side current is almost the same as the

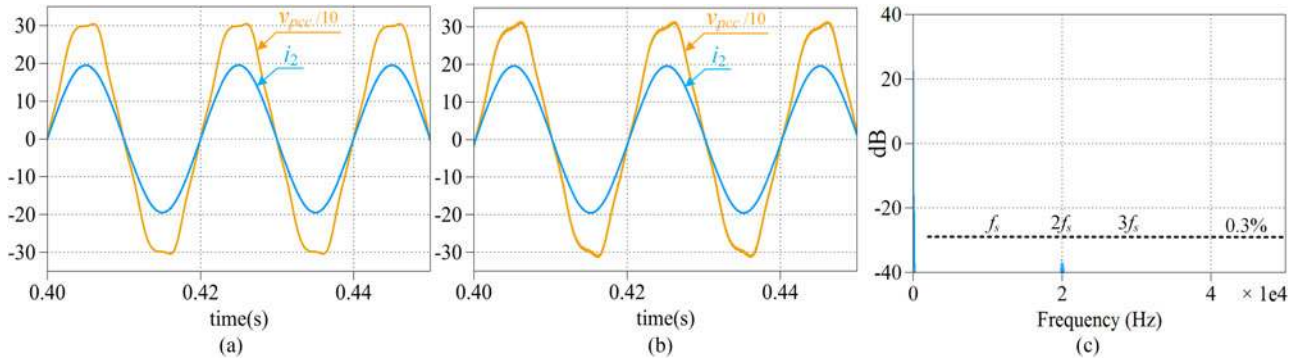

Fig. 13. Simulation steady-state results (a) $v_{\rm pcc}$ and i_2 waveforms with $L_g = 0$, (b) $v_{\rm pcc}$ and i_2 waveforms with $L_g = 3.7\,{\rm mH}$, and (c) i_2 spectrum.

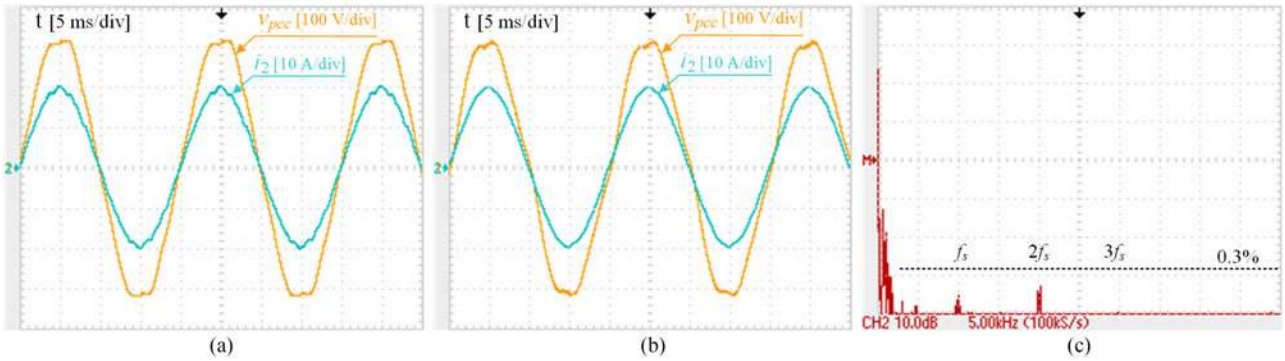

Fig. 14. Experimental steady-state results (a) $v_{\rm pcc}$ and i_2 waveforms with $L_g = 0$, (b) $v_{\rm pcc}$ and i_2 waveforms with $L_g = 3.7\,{\rm mH}$, and (c) i_2 spectrum.

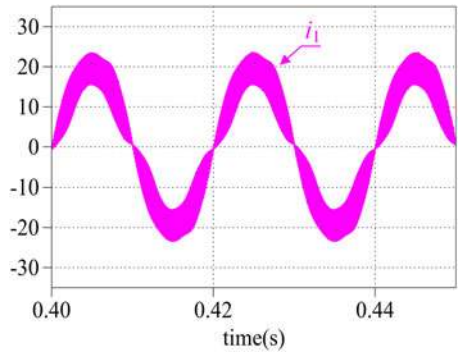

Fig. 15. Simulation waveform of converter current i_1.

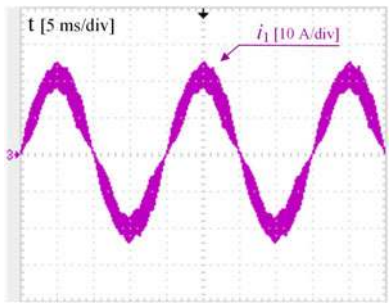

Fig. 16. Experimental waveform of converter current i_1.

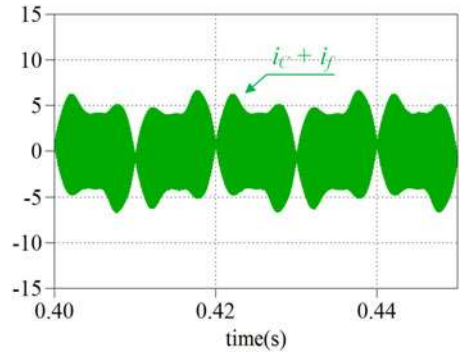

Fig. 17. Simulation waveform of $i_C + i_f$.

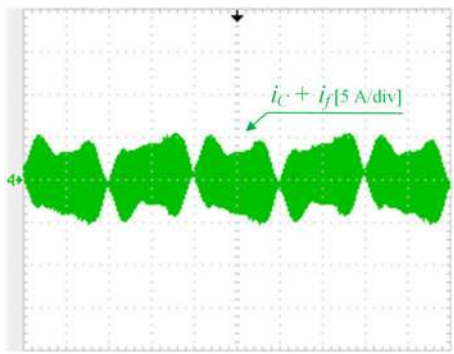

Fig. 18. Experimental waveform of $i_C + i_f$.

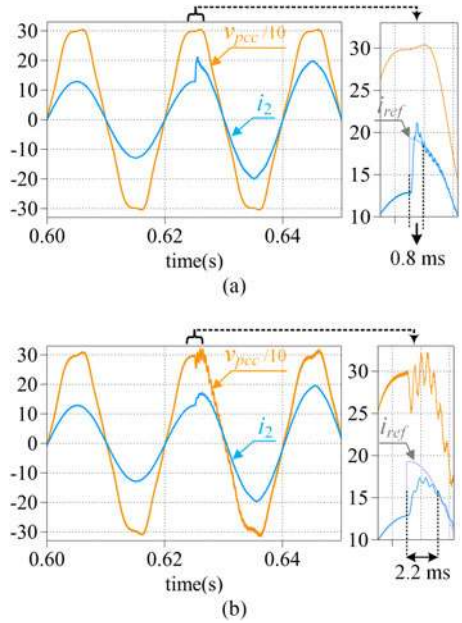

Fig. 19. Simulated dynamic response with active power jump from two-third to rated power (a) $L_g = 0$ and (b) $L_g = 3.7\,\mathrm{mH}$.

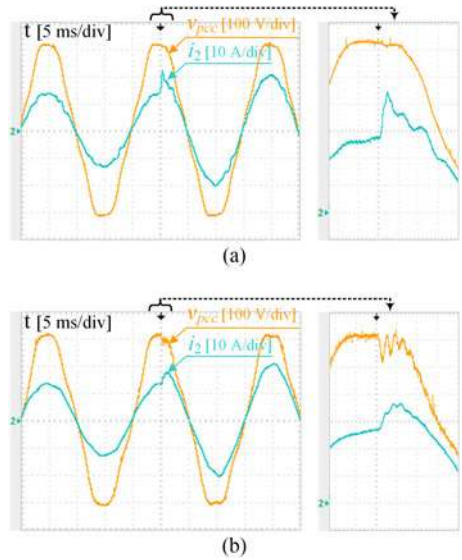

Fig. 20. Experimental dynamic response with active power jump from two-third to rated power (a) $L_g = 0$ and (b) $L_g = 3.7\mathrm{mH}$.

total current of parallel branches, $i_C + i_f$. As it can be seen in these waveforms, the maximum peak current ripple is about 5.8 A, which translates to 30% of the peak rated current, $I_{P,\mathrm{rated}}$.

In Figs. 19 and 20, a dynamic test is performed with a step in the reference active power from two-third to the rated power. Results confirm the excellent transient response with small oscillations. As described in Section V-B, with increasing L_g the value of ω_{gc} and consequently the dynamic response will decrease. As it can be seen, by increasing L_g from 0 to 3.7 mH the settling time of system increased form 0.8 to 2.2 ms.

In order to show the instability when the trap resonance is outside the recommended range of (7), simulation and experimental

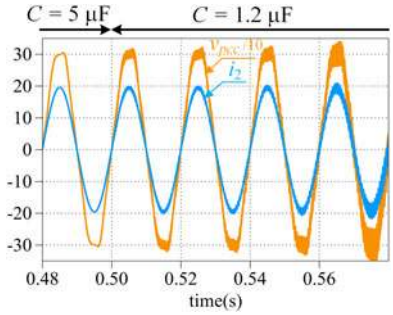

Fig. 21. Simulation results showing the instability when the trap resonance frequency is outside the stable range.

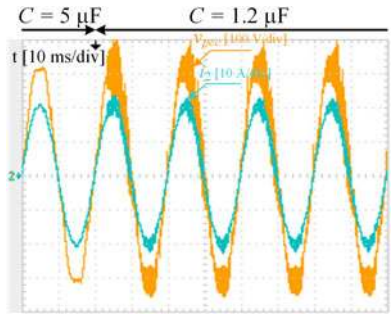

Fig. 22. Experimental results showing the instability when the trap resonance frequency is outside the stable range.

tests are performed. For the designed filter, by changing the filter capacitance (C) from 5 to 1.2 μF and considering $L_g = 200$ μH, the normalized resonance frequencies ($\omega_{\mathrm{res},0}/\omega_s$ and $\omega_{\mathrm{res},1}/\omega_s$) move from (0.33 and 1.21) to (0.46 and 1.79). According to (7) the instability occurs, since the trap resonance frequency, 1.79, is above the stable limit of (1+1/2 = 1.5). The simulation and experimental results for this case are shown in Figs. 21 and 22.

VII. Conclusion

In this paper, the folding effect of discretizing process, for all resonance frequencies of the *LCL-mT* filter has been investigated and based on the delay-based stabilization method, the stability condition for them all was determined. As an accurate base for the proposed design procedure, a general equation for the resonance frequencies of the *LCL-mT* filter without any approximations was developed. Then, a straightforward design algorithm for the *LCL-mT* filter was proposed, which guarantees robustness against grid inductance variations and parameter uncertainties. Additionally, in the proposed design method, the practical limits on filter parameters were also successfully addressed. The proposed design method was validated by simulation and experimental results.

Appendix

A. Capacitor Scaling According to the Reactive Power Limit

In order to redesign C and C_{f_1} without changing the resonance frequencies [i.e., satisfying both (16) and (17)], (18) must

be modified as

$$\begin{cases} C_{f1} = \left(1-(1/6)^2\right)\left((7/6)^2-1\right)u_{C,\max}C \\ C = xC_{\text{base}} - C_{f1} \end{cases}. \quad (27)$$

Then L_1 is recalculated from (18), as

$$L_1 = \frac{1}{u_{L,\max}u_{C,\max}C}\left(\frac{6^2}{7\omega_s}\right)^2. \quad (28)$$

The rest of the proposed design algorithm remains unchanged.

B. Extending the Design Procedure to the General Case of LCL-mT Filter With n Traps

At first, choose the minimum value of L_1 from (14). Through the same derivation as (15), considering $L_g = \infty$ and the maximum uncertainty factor $u_{\max}$, the minimum value for the ith resonance frequency can be calculated from (12) as

$$\omega^2_{\text{res},ia}\Big|_{\substack{L_g=\infty \\ u=u_{\max}}} = \frac{1}{u_{L,\max}L_1} \left(u_{C,\max}C + \sum_{j=1}^{n}\frac{C_{fj}}{1-L_{fj}C_{fj}\,\omega^2_{\text{res},ia}\Big|_{\substack{L_g=\infty \\ u=u_{\max}}}}\right)^{-1}, \quad i=0,1,\ldots,n. \quad (29)$$

To ensure stability for this case, each minimum resonance frequency must be at least equal to the lower limit of the stable range already defined by (7), i.e.,

$$\omega^2_{\text{res},ia}\Big|_{\substack{L_g=\infty \\ u=u_{\max}}} = \left(\left(i+\frac{1}{6}\right)\omega_s\right)^2. \quad (30)$$

Substituting (30) into (29), results in the following set of $n+1$ linear equations

$$\left(\left(i+\frac{1}{6}\right)\omega_s\right)^2 = \frac{1}{u_{L,\max}L_1}\left(u_{C,\max}C + \sum_{j=1}^{n}\frac{C_{fj}}{1-((i+1/6)/j)^2}\right)^{-1} \quad (31)$$

where $L_{fj}C_{fj}$ is replaced by $1/(j\omega_s)^2$. By expanding (31) for $i=0$ to n, a system of linear equations with $n+1$ unknowns is achieved. These equations must be simultaneously solved to give the values of all capacitors in the filter circuit.

With the same approach to derive (19), considering $L_g = 0$ and the minimum uncertainty factor $u_{\min}$, the maximum value for the ith resonance frequency can be calculated from (12) as

$$\omega^2_{\text{res},ia}\Big|_{\substack{L_g=0 \\ u=u_{\min}}} = \frac{\left(u_{C,\min}C + \sum_{j=1}^{n}\frac{C_{fj}}{1-L_{fj}C_{fj}\,\omega^2_{\text{res},ia}\Big|_{\substack{L_g=0 \\ u=u_{\min}}}}\right)^{-1}}{u_{L,\min}(L_1||L_2)}, \quad i=0,1,\ldots,n. \quad (32)$$

To ensure stability for this case, each maximum resonance frequency must be equal to (or lower than) the upper limit of the stable range already defined by (7), i.e.,

$$\omega^2_{\text{res},ia}\Big|_{\substack{L_g=0 \\ u=u_{\min}}} = \left(\left(i+\frac{1}{2}\right)\omega_s\right)^2. \quad (33)$$

Substituting (33) into (32) yields the following set of $n+1$ linear equations

$$\left(\left(i+\frac{1}{2}\right)\omega_s\right)^2 = \frac{\left(u_{C,\min}C + \sum_{j=1}^{n}\frac{C_{fj}}{1-((i+1/2)/j)^2}\right)^{-1}}{u_{L,\min}(L_1||L_2)}. \quad (34)$$

In above set of equations, all quantities are defined, except L_2. So, by solving (34) for $i=0$ to $n, n+1$ values for L_2 are calculated, where the maximum value must be chosen.

REFERENCES

[1] J. M. Carrasco, L. G. Franquelo, J. T. Bialasiewicz, E. Galvan, R. C. PortilloGuisado, M. A. M. Prats, J. I. Leon, and N. Moreno-Alfonso, "Power-electronic systems for the grid integration of renewable energy sources: A survey," *IEEE Trans. Ind. Electron.*, vol. 53, no. 4, pp. 1002–1016, Jun. 2006.

[2] F. Blaabjerg, R. Teodorescu, M. Liserre, and A. V. Timbus, "Overview of control and grid synchronization for distributed power generation systems," *IEEE Trans. Ind. Electron.*, vol. 53, no. 5, pp. 1398–1409, Oct. 2006.

[3] J. M. Bloemink and T. C. Green, "Reducing passive filter sizes with tuned traps for distribution level power electronics," in *Proc. 14th Eur. Conf. Power Electron. Appl.*, Aug./Sep. 2011, pp. 1–9.

[4] W. Wu, Y. He, and F. Blaabjerg, "An LLCL power filter for single-phase grid-tied inverter," *IEEE Trans. Power Electron.*, vol. 27, no. 2, pp. 782–789, Feb. 2012.

[5] J. Xu, J. Yang, J. Ye, Z. Zhang, and A. Shen, "An LTCL filter for three-phase grid-connected converters," *IEEE Trans. Power Electron.*, vol. 29, no. 8, pp. 4322–4338, Aug. 2014.

[6] F. Li, X. Zhang, H. Zhu, H. Li, and C. Yu, "An LCL-LC filter for grid-connected converter: Topology, parameter, and analysis," *IEEE Trans. Power Electron.*, vol. 30, no. 9, pp. 5067–5077, Sep. 2015.

[7] W. Wu, Y. He, T. Tang, and F. Blaabjerg, "A new design method for the passive damped LCL and LLCL filter-based single-phase grid-tied inverter," *IEEE Trans. Ind. Electron.*, vol. 60, no. 10, pp. 4339–4350, Oct. 2013.

[8] R. N. Beres, X. Wang, F. Blaabjerg, M. Liserre, and C. L. Bak, "Optimal design of high-order passive-damped filters for grid-connected applications," *IEEE Trans. Power Electron.*, vol. 31, no. 3, pp. 2083–2098, Mar. 2016.

[9] M. Hanif, V. Khadkikar, W. Xiao, and J. L. Kirtley, "Two degrees of freedom active damping technique for LCL filter-based grid connected PV Systems," *IEEE Trans. Ind. Electron.*, vol. 61, no. 6, pp. 2795–2803, Jun. 2014.

[10] Y. Liu, W. Wu, Y. He, Z. Lin, F. Blaabjerg, and H. S.-H. Chung, "An efficient and robust hybrid damper for LCL- or LLCL-based grid-tied inverter with strong grid-side harmonic voltage effect rejection," *IEEE Trans. Ind. Electron.*, vol. 63, no. 2, pp. 926–936, Feb. 2016.

[11] H. Komurcugil, S. Ozdemir, I. Sefa, N. Altin, and O. Kukrer, "Sliding-mode control for single-phase grid-connected LCL-filtered VSI with double-band hysteresis scheme," *IEEE Trans. Ind. Electron.*, vol. 63, no. 2, pp. 864–873, Feb. 2016.

[12] D. Pan, X. Ruan, C. Bao, W. Li, and X. Wang, "Capacitor-current-feedback active damping with reduced computation delay for improving robustness of LCL-type grid-connected inverter," *IEEE Trans. Power Electron.*, vol. 29, no. 7, pp. 3414–3427, Jul. 2014.

[13] D. Pan, X. Ruan, C. Bao, W. Li, and X. Wang, "Optimized controller design for LCL-type grid-connected inverter to achieve high robustness against grid-impedance variation," *IEEE Trans. Ind. Electron.*, vol. 62, no. 3, pp. 1537–1547, 2015.

[14] D. Yang, X. Ruan, and H. Wu, "a real-time computation method with dual sampling mode to improve the current control performance of the LCL-type grid-connected inverter," *IEEE Trans. Ind. Electron.*, vol. 62, no. 7, pp. 4563–4572, Jul. 2015.

[15] J. Dannehl, C. Wessels, and F. W. Fuchs, "Limitations of voltage-oriented pi current control of grid-connected PWM rectifiers with LCL filters," *IEEE Trans. Ind. Electron.*, vol. 56, no. 2, pp. 380–388, Feb. 2009.

[16] J. Dannehl, M. Liserre, and F. W. Fuchs, "Filter-based active damping of voltage source converters with LCL filter," *IEEE Trans. Ind. Electron.*, vol. 58, no. 8, pp. 3623–3633, Aug. 2011.
[17] A. Kahrobaeian and Y. A.-R. I. Mohamed, "Robust single-loop direct current control of LCL-filtered converter-based DG units in grid-connected and autonomous microgrid modes," *IEEE Trans. Power Electron.*, vol. 29, no. 10, pp. 5605–5619, Oct. 2014.
[18] J. Yin, S. Duan, and B. Liu, "Stability analysis of grid-connected inverter with LCL filter adopting a digital single-loop controller with inherent damping characteristic," *IEEE Trans. Ind. Informat.*, vol. 9, no. 2, pp. 1104–1112, May 2013.
[19] S. G. Parker, B. P. McGrath, and D. G. Holmes, "Regions of active damping control for LCL filters," *IEEE Trans. Ind. Appl.*, vol. 50, no. 1, pp. 424–432, Jan./Feb. 2014.
[20] C. Zou, B. Liu, S. Duan, and R. Li, "Influence of delay on system stability and delay optimization of grid-connected inverters with LCL filter," *IEEE Trans. Ind. Informat.*, vol. 10, no. 3, pp. 1775–1784, Aug. 2014.
[21] J. Wang, J. D. Yan, L. Jiang, and J. Zou, "Delay-dependent stability of single-loop controlled grid-connected inverters with LCL filters," *IEEE Trans. Power Electron.*, vol. 31, no. 1, pp. 743–757, Jan. 2016.
[22] Y. Tang, W. Yao, P. C. Loh, and F. Blaabjerg, "Design of LCL filters with LCL resonance frequencies beyond the Nyquist frequency for grid-connected converters," *IEEE J. Emerg. Sel. Topics Power Electron.*, vol. 4, no. 1, pp. 3–14, Mar. 2016.
[23] K. Ogata, *Discrete-Time Control Systems*, 2nd ed. Englewood Cliffs, NJ, USA: Prentice-Hall, 1995.
[24] M. Gopal, *Digital Control and State Variable Methods*, 3rd ed. New Delhi, India: McGraw-Hill, 2008.
[25] *IEEE Application Guide for IEEE Std. 1547, IEEE Standard for Interconnecting Distributed Resources With Electric Power Systems*, IEEE Standard 1547.2-2008, 2008.
[26] D. G. Holmes and T. A. Lipo, *Pulse Width Modulation for Power Converters: Principles And Practice*. Hoboken, NJ, USA: Wiley, 2003.
[27] A. G. Yepes, F. D. Freijedo, Ó. López, and J. Doval-Gandoy, "High-performance digital resonant controllers implemented with two integrators," *IEEE Trans. Power Electron.*, vol. 26, no. 2, pp. 563–576, Feb. 2011.
[28] X. Wang, F. Blaabjerg, and P. C. Loh, "Virtual RC damping of LCL-filtered voltage source converters with extended selective harmonic compensation," *IEEE Trans. Power Electron.*, vol. 30, no. 9, pp. 4726–4737, Sep. 2015.

Majid Sanatkar-Chayjani (S'12) received the B.Sc. degree in electrical engineering from Islamic Azad University, Borujerd, Iran, in 2009, and the M.Sc. degree (with honors) in electrical engineering from Ferdowsi University of Mashhad, Mashhad, Iran, in 2012, where he is currently working toward the Ph.D. degree.

His research interests include control of grid-connected converters, passive and active power filters, and power quality.

Mohammad Monfared (S'07–M'10–SM'15) received the B.Sc. degree in electrical engineering from Ferdowsi University of Mashhad, Mashhad, Iran, in 2004, and the M.Sc. and Ph.D. degrees (both with honors) in electrical engineering from Amirkabir University of Technology, Tehran, Iran, in 2006 and 2010, respectively.

He is currently an Associate Professor at Ferdowsi University of Mashhad, where he received the Best Researcher Award in 2015. His research interests include power electronics, renewable energy systems, and power quality.